Superconductor Science and Technology

PAPER

Enhanced higher temperature irreversibility field and critical current density in MgB_2 wires with Dy_2O_3 additions

To cite this article: Y Yang *et al* 2021 *Supercond. Sci. Technol.* **34** 025010

IOP Publishing Superconductor Science and Technology
Supercond. Sci. Technol. **34** (2021) 025010 (12pp) https://doi.org/10.1088/1361-6668/abc73c

Enhanced higher temperature irreversibility field and critical current density in MgB_2 wires with Dy_2O_3 additions

Y Yang[1,2], M D Sumption[1], M Rindfleisch[3], M Tomsic[3] and E W Collings[1]

[1] Center for Superconducting and Magnetic Materials, Department of Materials Science and Engineering, the Ohio State University, Columbus, OH 43210, United States of America
[2] Western Digital, San Jose, CA, United States of America
[3] HyperTech Research Inc, Columbus, OH 43228, United States of America

E-mail: sumption.3@osu.edu

Received 13 August 2020, revised 15 October 2020
Accepted for publication 3 November 2020
Published 12 January 2021

Abstract

Bulk samples of magnesium diboride (MgB_2) doped with 0.5 wt% of the rare earth oxides (REOs) Nd_2O_3 and Dy_2O_3 (named B-ND and B-DY) prepared by standard powder processing, and wires of MgB_2 doped with 0.5 wt% Dy_2O_3 (named W-DY) prepared by a commercial powder-in-tube processing were studied. Investigations included x-ray diffractometry, scanning- and transmission electron microscopy, magnetic measurement of superconducting transition temperature (T_c), magnetic and resistive measurements of upper critical field (B_{c2}) and irreversibility field (B_{irr}), as well as magnetic and transport measurements of critical current densities versus applied field ($J_{cm}(B)$ and $J_c(B)$, respectively). It was found that although the products of REO doping did not substitute into the MgB_2 lattice, REO-based inclusions resided within grains and at grain boundaries. Curves of bulk pinning force density (F_p) versus reduced field ($b = B/B_{irr}$) showed that flux pinning was by predominantly by grain boundaries, not point defects. At all temperatures the $F_p(b)$ of W-DY experienced enhancement by inclusion-induced grain boundary refinement but at higher temperatures $F_p(b)$ was still further increased by a Dy_2O_3 additive-induced increase in B_{irr} of about 1 T at all temperatures up to 20 K (and beyond). It is noted that Dy_2O_3 increases B_{irr} and that it does so, not just at 4 K, but in the higher temperature regime. This important property, shared by a number of REOs and other oxides promises to extend the applications range of MgB_2 conductors.

Keywords: MgB_2, B_{irr}, B_{c2}, Dy_2O_3, J_c

(Some figures may appear in colour only in the online journal)

1. Introduction

Magnesium diboride, MgB_2, is a promising superconductor for applications at intermediate temperatures around 15–20 K. Since it is not afflicted by grain boundary weak-link problems MgB_2 can be used in its polycrystalline form which significantly reduces the complexity and cost of large scale conductor fabrication. As a result multifilamentary MgB_2 wires have been considered for numerous applications. But to extend the promise of MgB_2 for practical applications an increase in the high field critical current density, J_c, is needed. Several approaches address this issue: (a) doping with carbon containing materials [1–6] to enhance the upper critical field, B_{c2}. (b) Introduction of new flux pinning centers to increase the bulk pinning force density, F_p, and J_c by, for example, neutron irradiation [7] and grain refinement [8]. (c) Improvement of the intergrain connectivity by cold- or hot pressing [9, 10] and by the use of improved wire-processing techniques such

as internal magnesium diffusion [11–13]. (d) Chemical doping with selected dopant species other than C that alloy with MgB_2 to enhance B_{c2} [2–7] and/or induce defects and precipitates to increase flux pinning [14–19]. However, chemical doping may also induce impurities that reduce connectivity and hence J_c. Therefore, the balance between the benefit of enhanced B_{c2} and J_c and the trade-off of reduced connectivity must be considered when selecting a dopant for MgB_2. Several studies have shown that small percentages of nano-sized rare earth oxide (REO) powders of Dy_2O_3 [13, 14], Nd_2O_3 [16], Ho_2O_3 [17, 19], Pr_6O_{11} and Eu_2O_3 [18], can enhance the superconducting properties of MgB_2. A very nice summary of some of the results for a whole variety of REO additions is given in [20], including increments in B_{irr}. Here and elsewhere, Dy_2O_3 has been seen to be one of the better performing oxides additions. To further investigate the effects of REO doping in high performing *in situ* materials, we initiated the detailed investigation of Dy_2O_3 and Nd_2O_3 added MgB_2 bulks and wires described below. We found that some properties responded to the addition of these dopants and others did not, at least at the levels explored in this work. Those non-responsive to 0.5% Dy_2O_3 doping included (a) lattice parameter, a and c (b) superconducting transition temperature, T_c, and (c) Upper critical field, B_{c2}. On the other hand, those responsive to doping included: (a) grain size, D, (b) the development of precipitates and inclusions, (c) Kramer- and irreversibility fields, B_k and B_{irr}, (d) critical current density, J_c, and the associated bulk pinning force density, F_p, (e) pinning force density and grain size in bulks and wires, and (f) temperature dependence of pinning force density.

The x-ray diffraction (XRD) data and the results of T_c measurement indicate that the products of REO doping after heat treated (HT) do not substitute into the MgB_2 lattice. Electron microscopy reveals REO-based inclusions at grain boundaries and within grains. The form of the $F_p(b)$ curves indicate that the while in principle way may expect the inclusions to act as point-defect pinning sites, there was not a noticeable point pinning signature generated by the Dy_2O_3 additions; possibly the defect density was too low. Pinning by grain boundaries is indicated by the form of the $F_p(b)$ curves and also by the proportionality of $F_{p,max}$ to reciprocal grain size, $1/D$. We deduce that the grain-boundary inclusions inhibit grain growth (via, e.g. a Zener pinning mechanism for grain refinement) during HT and are responsible for the observed doping-induced J_c, and $F_p(b)$, improvements at 4 K. At higher temperatures (20–25 K) an additional J_c-enhancement mechanism comes into play. But beyond J_c-enhancement it is important to note that Dy_2O_3 increases B_{irr} and that it does so, not just at 4 K, but in the higher temperature regime. This also happens for a number of other REOs and metalloid oxides. In fact experiment evinces a Dy_2O_3-doping-induced B_{irr} increase of ~1 T at all temperatures up to 20 K (and beyond). Although B_{c2} was found to remain fixed (see section 3.3) the observed increase in B_{irr} implies a reduction in magnetocrystalline anisotropy as gauged by the parameter $(B_{c2}-B_{irr})/B_{c2}$ which translates into an increase in connectivity and hence J_c.

2. Experimental

2.1. Sample preparation

2.1.1. Bulks. Three bulk samples were fabricated: (i) pure MgB_2 bulk B-00 made by mixing Mg powder (99%, <44 μm particle size) and B powder (99%, from Alpha Aesar) according to the molar ratio of Mg:B = 1.1:2; (ii) Dy_2O_3 added bulk B-DY made by adding 0.5 wt% Dy_2O_3 powder (>99.9%, <100 nm particle size, Aldrich); and (iii) Nd_2O_3 added bulk B-ND made by adding 0.5 wt% Nd_2O_3 powder (>99.9%, <100 nm particle size, Aldrich). After 1 h grinding in a mortar, the mixture was uniaxially pressed into ~4 mm tall by ~8 mm diameter pellets, capsulated in quartz tubing under Ar and HT for 30 min at 700 °C.

2.1.2. Wires. Monofilamentary wires, manufactured by the commercial tube-forming-and-filling (CTFF) process [21], were provided by HyperTech Research Inc. The 8.3 mm diameter wires included chemical barriers of Nb and outer sheaths of monel. Commercial Mg powder (99%, <44 μm particle size) and 2 at% C pre-doped SMI boron from Specialty Metals Inc. (SMI) were used [22]. Two types were fabricated: (i) MgB_2 wires with no Dy_2O_3 additions, labeled W-00; (ii) 0.5 wt% Dy_2O_3 nano-powder added MgB_2 wires labeled W-DY. The wire samples were encapsulated in quartz tubing under Ar and HT for 30 min at 650 °C, 675 °C and 700 °C. Superconductive property measurements were confined to the wires HT for 30 min at 675 °C^{-1}. Sample information is listed in table 1.

2.2. Measurements

2.2.1. Bulks. (1) Magnetization-vs-field, $M(B)$, measurements were made on cuboid-shaped samples using a Quantum Design Model 6000 PPMS at temperatures of 4.2 K to 20 K and at available fields of ±10 T. The magnetic critical current densities, J_{cm}, of the bulks were calculated based on Bean's critical state model:

$$J_{cm} = \frac{3\Delta M}{b\left(1 - b/3a\right)} \quad (1)$$

where ΔM is the width of the hysteresis loop at a given B, a is the length of the sample's longer edge and b that of its shorter edge. Both a and b are orthogonal to B. The bulk pinning force density, $F_p = J_{cm} \times B$, the Kramer irreversibility field, B_k, (based on extrapolations of ${J_{cm}}^{0.5}B^{0.25}$ versus B) and the upper critical field, B_{c2}, were also derived from the magnetization results. The superconducting critical transition temperature T_c and the T_c distribution were determined from the temperature dependence of DC magnetic susceptibility. (2) XRD analysis was performed on the bulk samples using a Rigaku MiniFlex 600 with Cu K_α = 1.5418 Å with scanning angles 2Δ of from 20° to 80°. (3) An FEI/Philips Sirion scanning electron microscope (SEM) with a field-emission source and a

Table 1. Doping additions, 30 min HT temperatures, lattice parameters, RE contained impurities, and grain sizes.

Sample	Dopant additions	HT temperatures	a (Å)	c (Å)	RE boride impurities	D (nm)
B-00	None	700 °C	3.082(8)	3.522(1)		463
B-DY	0.5 wt% Dy_2O_3	700 °C	3.082(3)	3.520(8)	DyB_4	312
B-ND	0.5 wt% Nd_2O_3	700 °C	3.081(9)	3.519(2)	NdB_6	223
		650 °C				55
W-00	2 at% C	675 °C				134
		700 °C				215
		650 °C				59
W-DY	2 at% C + 0.5 wt% Dy_2O_3	675 °C				99
		700 °C				151

through-the-lens (TTL) detector was used for microstructural imaging and grain size measurement. (4) Transmission electron microscope (TEM) imaging was performed using a FEI/-Philips CM-200 T (TEM) with a silicon drift detector and its energy-dispersive x-ray spectroscopy function. B-DY and B-ND samples were prepared by grinding to a fine powder for ~10–20 min using an agate mortar and pestle. A small amount (<1 mg) of the ground powder was placed into a glass vial, mixed with isopropanol, and ultrasonicated to a uniform dispersion of MgB_2 particles. A small quantity of this dispersion was pipetted out, dripped onto a lacey carbon TEM grid, and allowed to dry.

2.2.2. Wires. (1) Transport measurements of critical current density, J_{ct}, and transport irreversibility field (B_{irr}, based a $J_c = 10^3$ A cm^{-2} criterion) were made on strands prepared in the form of 'short samples' (3 cm in length with a voltage-tap gauge length of 5 mm) at 4.2 K in pool-boiling liquid He in transverse magnetic fields of from 0 to 13 T. (2) Magnetic (i.e. *M*-*B*-based) measurements of critical current density, J_{cm}, were made using the Quantum Design Model 6000 PPMS. The magnetic J_{cm} versus applied transverse field, B, was calculated according to:

$$J_{cm} = \frac{3\pi\Delta M}{4d} \tag{2}$$

where ΔM is the width of the magnetization-hysteresis loop at a given B, and d is the diameter of the wire's superconducting core. The low-field results enabled J_{cm} (= J_c, see later) to be extrapolated to low fields inaccessible to transport measurement. These and the high-field results allowed the completion of set of bulk pinning force density, F_p, curves for the wire samples. (3) Resistance versus decreasing temperature measurements were made under various transverse magnetic fields. The resulting upper critical field, B_{c2}, and irreversibility field, B_{irr}, were defined as the fields corresponding to 90% and 10%, respectively, of the normal state resistance. The B_{c2} and B_{irr} data below 13 T were measured at our Center for Superconducting and Magnetic Materials (CSMM) and those above 13 T at the National High Magnetic Field Laboratory (NHMFL). (4) The microstructures of fractured samples of W-00 and W-DY HT at various temperatures were revealed by secondary electron (SE) imaging and grain size measurements were made.

3. Results

3.1. XRD and lattice parameters, a and c

The XRD data for B-00, B-ND, and B-DY are presented in figure 1 where the Bragg reflections are indexed for only the MgB_2 phase for simplicity. All samples contained MgO as impurities. No peak shifts at (110) and (002) were observed in either of the doped samples. The lattice parameters extracted from pseudo-Voigt fitting the MgB_2 peak reflections are listed in table 1. Both lattice parameters a and c remained unchanged after REO doping (unlike the results of C doping [5]). It can be concluded that Dy_2O_3 and Nd_2O_3 or their possible decomposition products did not substitute into the MgB_2 lattice to an extent detectable by XRD.

3.2. Superconducting transition temperatures, T_c

The superconducting transition temperatures (T_c) and T_c distribution of B-00, B-ND, and B-DY were obtained by DC-susceptibility (χ) measurement, figures 2(a) and (b). The T_c was defined as the onset of superconductivity from the normal state at 10 mT and the T_c distribution was expressed in terms of dχ/dT. The onset T_cs and the full-widths at half maximum (FWHM) of all samples are listed in table 2. The undoped sample B-00 shows a very sharp superconducting transition with a T_c of 39.2 K and a FWHM of ~0.4 K. The T_cs did not change after adding Dy_2O_3 and Nd_2O_3. A small increase (~0.1 K) in FWHM was observed in B-DY, while the FWHM of B-ND was unchanged. Unlike substitutional doping with Al or C which cause notable changes of T_c, our REO doping did not alter the T_c of MgB_2 and had only small effects on the T_c distribution. Again, these observations suggest that Dy_2O_3 and Nd_2O_3 doping did not result in elemental substitution for Mg or B atoms during reaction.

3.3. Upper critical fields, B_{c2}

The temperature dependencies of the upper critical fields, B_{c2}, of B-00, B-ND, and B-DY were obtained by magnetization measurement at CSMM, those of W-00 and W-DY were measured resistively at CSMM and the NHMFL. The results, presented in figures 3(a) and (b) and table 5 indicate that the B_{c2}s were practically unaffected by REO doping.

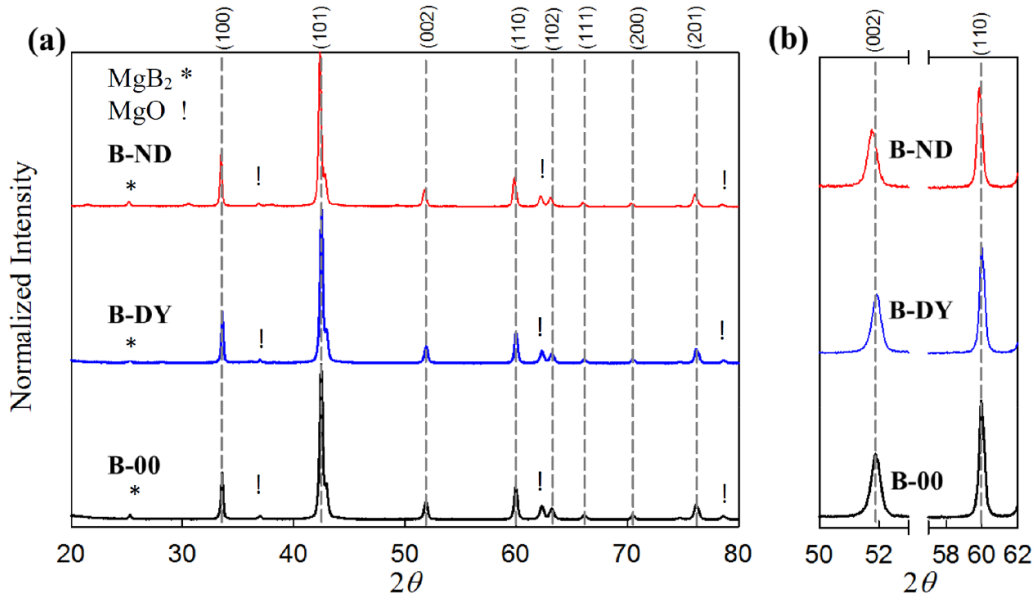

Figure 1. (a) X-ray diffraction patterns of undoped MgB_2 sample B-00, and all the REO doped bulk samples. (b) Enlargement of the peaks (110) and (002), which are directly related to the lattice parameters *a* and *c,* respectively. No peak shifting is observed for the REO doped samples.

Table 2. Superconducting properties of MgB_2 bulks.

Sample	Onset T_c (K)	FWHM of T_c (K)	B_k (T) 4.2 K	10 K	20 K	b_{peak} at 10 K	$F_{p,max}$ (GN m^{-3}) at 10 K	Grain size, *D* (nm) after 30 min at 700 °C^{-1}
B-00	39.2	0.4	7.72	6.57	5.56	0.2	0.49	463
B-DY	39.2	0.5	7.87	6.86	5.89	0.21	0.66	312
B-ND	39.2	0.4	7.84	6.85	5.87	0.23	0.93	223

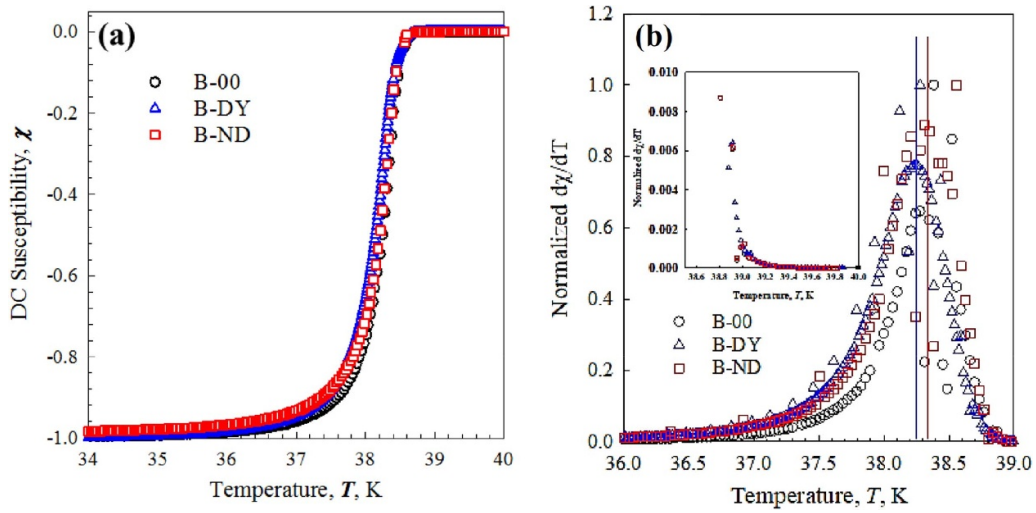

Figure 2. (a) DC susceptibility χ versus T at 0.01 T; (b) the T_c distribution in terms of dχ/dT versus T.

3.4. Grain sizes, D

3.4.1. Bulks. The fracture SE images of the REO doped bulks, taken by TTL detection, are presented in figures 4(a)–(c). Most of the grains in these three traditional bulks had a hexagonal plate-like shape interspersed with small spherical grains located in micro-voids between them. The size of these hexagonal plate-like MgB_2 grains was expressed in terms of an average diameter, *D*, according to:

Table 3. Superconducting properties of MgB_2 wires.

Sample	J_{ct} at 12 T and 4.2 K ($A°cm^{-2}$)	B_k (T) 4.2 K	10 K	20 K	$F_{p,max}$ ($GN°m^{-3}$) 4.2 K	10 K	20 K	Grain size, D (nm) after 30 min at 700 °C^{-1}	b_{peak} at 10 K
W-00	4.2×10^3	9.91	8.02	5.1	9.34	5.85	2.19	215	0.20
W-DY	1.7×10^4	10.44	8.72	5.55	10.11	6.78	3.37	151	0.23

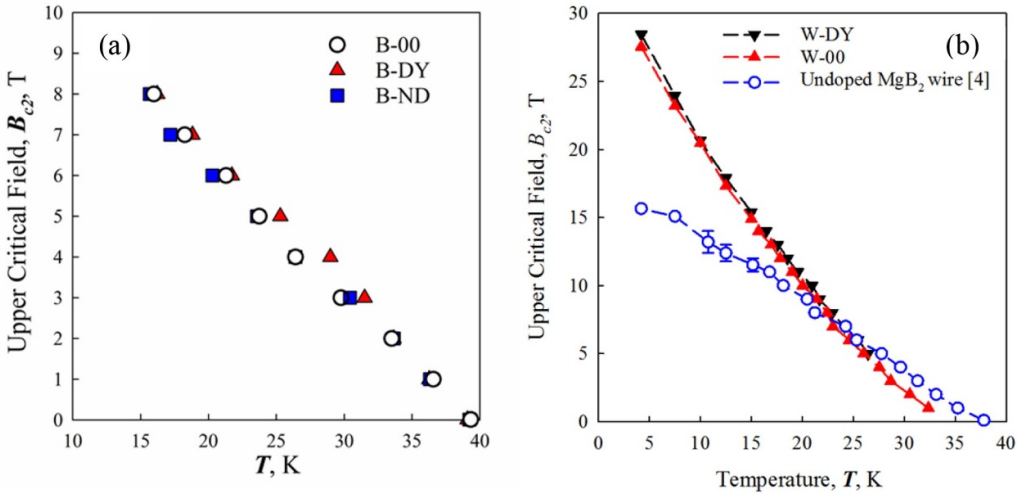

Figure 3. Upper critical fields B_{c2} versus temperature of (a) the bulks B-00, B-ND, and B-DY and (b) the wires W-00 and W-DY. Data for a wire with no Dy_2O_3 additions and no C-doping [4] is shown as blue open circles.

Table 4. B_{irr} (transport, figure (8)) for W-00 and W-DY. Values for the 2 wt% Dy_2O_3/C co-doped MgB_2 AIMI wire D3 of [13] are listed for comparison.

Strand name	W-OO	W-DY	D3
Dopant level, wt%	0	0.5	2.0
10 K	12	13.8	14.7
15 K	9.7	11	11.4
20 K	7	8.3	8.2
25 K	4	5	4.9

Table 5. $F_{p,max}$ (10 K) and grain size for all samples.

Sample	$F_{p,max}$,10 K, GN m^{-3}	B_{c2}, 10 K T	D^a, nm	$1/D$ $10^6 m^{-1}$	p, N m^{-2}
B-00	0.49	10	463	2.16	227
B-DY	0.66	10	312	3.21	206
B-ND	0.93	10	223	4.48	207
W-00	5.9	20.5	134	7.46	790
W-DY	6.83	20.5	99	10.10	676

[a] Bulks HT 30 min at 700 °C^{-1}; wires HT 30 min at 650 °C^{-1}.

$$D = \frac{2\sum\sqrt{A_i/\pi}}{N} \quad (3)$$

where N is the total number of grains in the examined area, and A_i is the area of the ith grain. The values of D for the bulk samples are listed in table 1. The hexagonal plate-like MgB_2 grains of the REO doped samples were significantly smaller than those of the undoped bulk B-00.

3.4.2. Wires. The microstructures of W-00 and W-DY HT at various temperatures were revealed by fracture SE imaging, figure 5, and the grain sizes were evaluated as described above. For the undoped W-00 after a HT at 30 min at 650 °C^{-1} most of the MgB_2 consisted of loosely connected fine spherical grains with a size of ~55 nm along with a small amount of coarser grains, figure 5(a). For a HT of 30 min at 675 °C^{-1} most of the grains coarsen into hexagonal plate-like grains (134 nm), figure 5(b). The intergranular connections strongly improve although some nano-size voids can still be observed. At a HT of 30 min at 700 °C^{-1} most of the MgB_2 grains exist as coarse, well connected, hexagonal plates with an average size of about 215 nm, figure 5(c).

In the Dy_2O_3 doped wire W-DY, fine spherical fine grains with a size of ~59 nm formed during a HT of 30 min at 650 °C^{-1}, figure 5(d). For a HT of 30 min at 675 °C^{-1}, the grains were again mostly fine and spherical (unlike for W-00), although coarse plate-like MgB_2 grains (~99 nm) existed in thin (~1 μm thick) MgB_2 layers surrounding voids, figure 5(e). For HT of 30 min at 700 °C^{-1}, the thickness of the coarse grain (~151 nm) MgB_2 layers increased somewhat (~2 μm) and all the fine spherical grains transformed into hexagonal plate-like

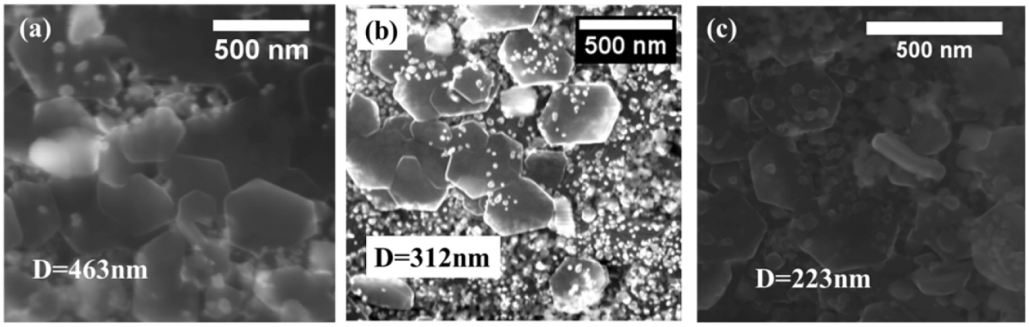

Figure 4. (a) Secondary electron imaging (SE) by through-the-lens detection (TLD) on a fractured surface of B-00. Some MgB_2 grains are dimensioned; (b) a fractured surface of B-DY; (c) a fractured surface of B-ND. Note that the grains in the REO-doped samples are smaller than those in undoped B-00.

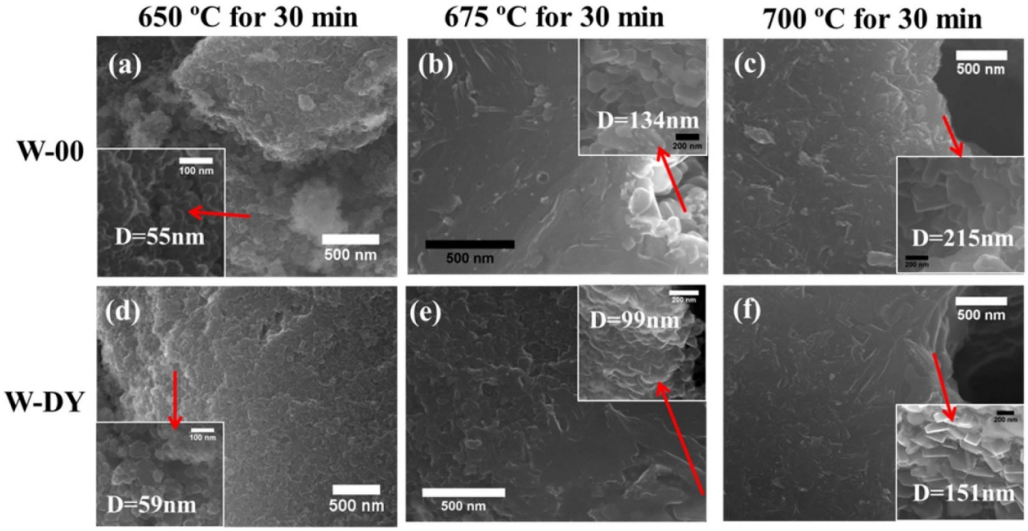

Figure 5. Secondary electron imaging (SE) by through-the-lense detection (TLD) on fractured surfaces of W-00 and W-DY. Three heat treatments were administered: (a)/(d) 30 min at 650 $°C^{-1}$, (b)/(e) 30 min at 675 $°C^{-1}$, (c)/(f) 30 min at 700 $°C^{-1}$. Insets are enlarged SEM images.

MgB_2 grains which were still smaller than those in the MgB_2 layers, figure 5(f).

The results indicate that Dy_2O_3 inhibits MgB_2 grain coarsening in both the wire W-DY and the bulk B-DY. In particular, after HT 30 min at 700 $°C^{-1}$ the grain size of W-DY was 30% less than that of W-00, and the grain size of B-DY was 33% less than that of B-00. The influences of Dy_2O_3 doping on the grain sizes of bulks and wires HT 30 min at 700 $°C^{-1}$ are summarized in tables 2 and 3. It is useful to note that even through the bulks and wires were processed using different sources of B (crystalline micro-size B in the bulks and C-doped amorphous SMI nano-size B in the wires) grain refinement with Dy_2O_3 additions is present at some level in both.

3.5. Precipitates and inclusions

Figures 6(a), (b), (c) and (d) are bright-field TEM images obtained from fine powders of B-DY and B-ND. Inclusions 20–50 nm in size were observed inside the MgB_2 grains and some larger inclusions (>50 nm) were found outside them. These are expected to be DyB_4, based on the known reduction of Dy_2O_3 with B [23], and previous work on Dy_2O_3 additions in MgB_2 [14]. Our precipitates seemed to be somewhat larger and more widely spaced that those seen in Chen [14], although this bears confirmation with higher resolution TEM. Perhaps for this reason, the in-grain nano-inclusions did not seem to provide point pinning (see section 3.7). In principle we would expect the addition of some point pinning character to the flux pinning response, it may be that we have a relatively low density of precipitates and this point pinning signature is too weak to be evident. However, the nano-inclusions found at grain boundaries would be expected to inhibit grain growth and suppressed grain coarsening during HT (Zener pinning). This observation provides an explanation for the grain refinement noted in the REO-doped bulks, tables 2 and 5.

3.6. Irreversibility fields, B_k and B_{irr}

The Kramer irreversibility fields, B_k, of the bulks B-00, B-ND, and B-DY were obtained by extrapolation of the magnetically derived plots of $J_{cm}{}^{0.5}B^{0.25}$ versus B, figure 7. The resulting

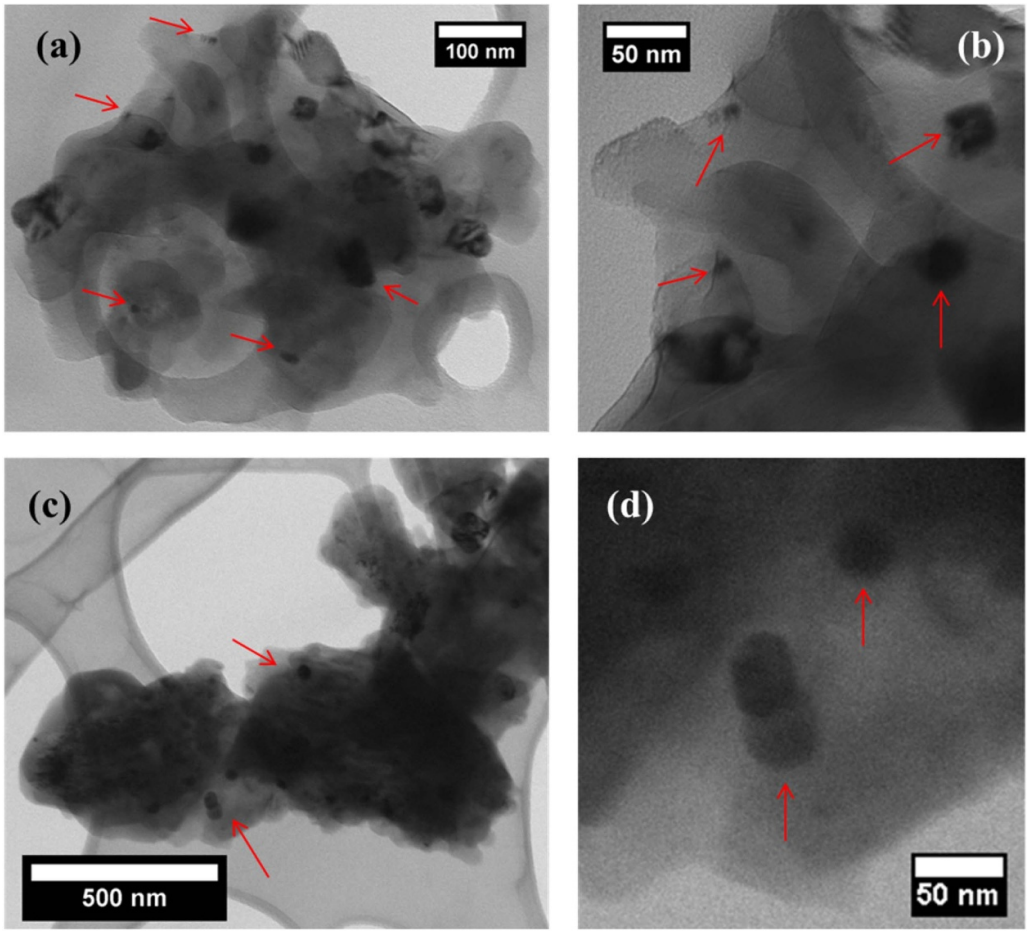

Figure 6. Bright-field (BF) TEM imaging of: (a) an agglomeration inside grains of B-DY; (b) nano-size inclusions inside grains of B-DY; (c) an agglomeration inside grains of B-ND; (d) nano-size inclusions inside grains of B-ND.

B_k values at 4.2 K, 10 K, and 15 K are presented in table 2. Two techniques were applied to the measurement of the irreversibility field B_{irr} of W-00 and W-DY: (i) one is the field under which the extrapolated transport $J_c(B)$ drops to $J_c = 10^3$ A cm^{-2}; the resulting 'transport B_{irr}' data for W-00 and W-DY are plotted in figure 8 and tabulated (for 10–25 K) in table 4. (ii) Another is the field in which the wire's resistance as a function of decreasing field is 10% below its normal-state value; the resulting 'resistive B_{irr}s' of W-00 and W-DY are also plotted versus temperature in figure 8. Both B_k and B_{irr} increase in response to the addition of dopant. For example, after the addition of 0.5 wt% Dy_2O_3 $B_{k,15\ K,bulk}$ increased 0.33 T, $B_{k,20\ K,wire}$ increased 0.45 T, $B_{irr,15\ K,wire}$ and $B_{irr,20\ K,wire}$ both increased 1.3 T.

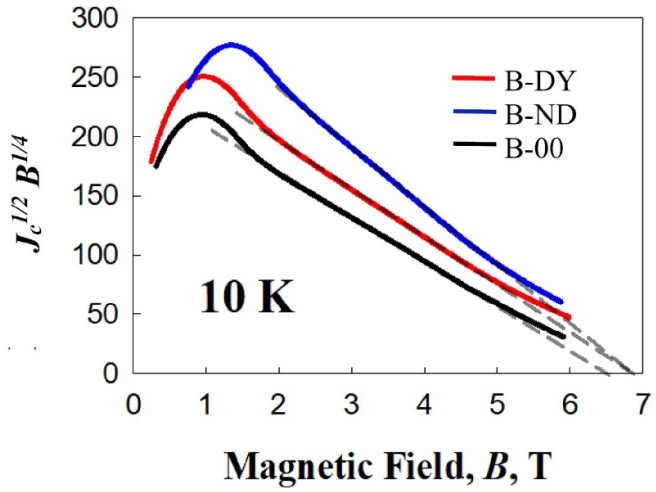

Figure 7. Kramer plot $J_c^{0.5}B^{0.25}$ versus B based on magnetic critical current density J_{cm} versus B for the bulks B-00, B-ND, and B-DY.

3.7. Critical current density, J_c, and the associated bulk pinning force density, F_p

The transport measured J_c (1 μV cm^{-1} criterion) and the magnetic J_{cm} (based on equation (4)) are plotted versus field (at temperatures 4.2–20 K) in figures 9(a) and (b). It can be seen that the addition of Dy_2O_3 increases both transport and magnetic J_c over a large range of temperature and field. Comparing these figures it can be seen that although J_{cm} approximates J_c in fields below about 5 T it drops rapidly below J_c in higher fields. As explained in detail elsewhere [24] J_{cm} is a sample-aspect-ratio-dependent combination of the longitudinal J_c and J_{trans}, a critical current density transverse to the wire axis. This J_{trans} can be neglected at low fields where it allows $J_m - J_c$,

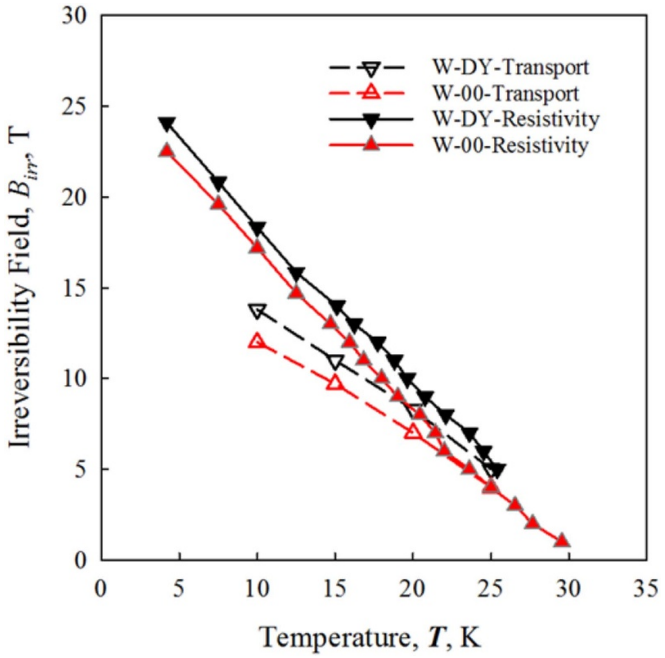

Figure 8. Irreversibility fields B_{irr} versus T for the wires W-00 and W-DY. The filled symbols are from resistivity measurement and the unfilled symbols represent transport B_{irr} obtained from the data of figure 9(a) extrapolated to $J_c = 10^3$ A cm^{-2}.

but at high fields its introduction causes a rapid drop-off of J_m – and, by the way, causes the difference between $B_{irr,20\,K,wire}$ (8.3 T) and $B_{k,20\,K,wire}$ (5.55 T).

The sources of the pinning force density curve, $F_p(b)$, of figure 10(a) are the $J_{cm}(B)$ data of figure 9(b) at 4.2 K, 10 K, and 20 K and the corresponding $b = B/B_{k,wire}$ values. We see the J_c increases with Dy_2O_3 additions translated into increases in F_p. The low field magnetic data ($J_{cm} - J_c$) enabled the peak of the F_p curve to be reliably traced (and could be reasonably regarded as transport-based) while the high field regions (based on J_{cm} and not J_c) are irrelevant to this discussion. As shown by Dew-Hughes [25] and Kramer [26], in response to normal surface pinning (e.g. grain-boundary, GB pinning), $F_p(b)$ maximizes at $b = 0.2$ according to:

$$F_p = 3.494 F_{p,max} b^{1/2} (1-b)^2 \quad (4)$$

In figure 10(b) the plots of $f_p = F_p/F_{p,max}$ versus at 4.2 K, 10 K, and 20 K all maximize close to $b_{max} = 0.2$ indicating that grain boundaries, not point defects, are mostly responsible for flux pinning in W-00 and W-DY. The same is true for the bulks B-00, B-ND, and B-DY with $b_{max,10\,K}$ values of 0.2, 0.23, and 0.21, respectively, see table 2 and figure 10(c). Values of $F_{p,max,bulk,10\,K}$ from the data of figure 10(c) when plotted versus reciprocal grain size, $1/D$, as in figure 11 verify the well-known relationship

$$F_{p,max} \alpha\, 1/D \quad (5)$$

3.8. Pinning force density and grain size in bulks and wires

In this section we discuss the relationship between $F_{p,max}$ and grain size for bulks and wires based on equation (5), $F_p \alpha\, 1/D$. Instead of the proportionality we introduce a factor p such that $F_{p,max} = p/D$. As shown in figure 12, $F_{p,max}$ versus $1/D$ produces two lines, one of slope p_B (for bulks prepared using pure B powder) and the other of slope p_W (for wires based on 2 at% pre-doped SMI B). The ratio of the slopes, $p_W/p_B = 3.40$, is attributed to the effect of C substitution on B_{c2} and the Ginzburg-Landau (GL) parameter, κ.

According to [22] the $F_{p,max}$ of equation (4) can be expressed in the form:

$$F_{p,max} = C_s {B_{c2}}^{2.5}/\kappa^2 \quad (6)$$

in which C_s is a microstructure-dependent parameter. As indicated above C_s under GB pinning should be proportional to $1/D$ and hence:

$$p\, \alpha\, {B_{c2}}^{2.5}/\kappa^2 \quad (7)$$

Using the $B_{c2,10\,K}$ values from figure 3(a) ($B_{c2,10\,K,Bulk} = 10$ T) and 3(b) ($B_{c2,10\,K,Wire} = 20.5$ T) and equating p_W/p_B based on equation (7) to the above experimentally obtained $p_W/p_B = 3.40$ we find $\kappa_W/\kappa_B = 1.33$. This 25% increase in the GL parameter we attribute to scattering by the C doping. A comparable increase of $\kappa = B_{c2}/2^{1/2}B_c$ in response to C doping can be deduced with the aid of B_c data published by Mudgel *et al* [27] who reported that for 0 and 4 at% C doping, $B_{c,0\,K}(0\%\,C)/B_{c,0\,K}(4\%\,C) = 15.7\,T/23.2\,T = 0.68$. Combining this with the above B_{c2} ratio (= 2.05) it follows that $\kappa_W/\kappa_B \sim 1.39$, which is consistent with our results.

3.9. Temperature dependence of pinning force density

The field dependencies of F_p at 4.2 K, 10 K, and 20 K for W-00 and W-DY are compared in figure 10(a). Not only does $F_p(b)$ increase overall with the addition of Dy_2O_3 but the increase is strongly temperature dependent. For example at 4.2 K, 10 K, and 20 K, increases in $F_{p,max}$ (i.e. $\Delta F_{p,max}$) of 8%, 16%, and 54%, respectively, are seen in figure 10(a) and reported in table 3. The forms of $F_p(b)$ and other evidence presented above prove that all the undoped and doped bulks and wires are grain-boundary pinners, in response to which the percentage increases in $\Delta F_{p,max}$ should be independent of temperature. Let us assume as a starting point that the $\Delta F_{p,max}$ (viz. 8%) at 4.2 K is entirely due to a Dy_2O_3-induced increase in grain boundary pinning. Then after applying this 8% to the $F_{p,max}$s of W-00 at 10 and 20 K and comparing the results with the observed $F_{p,max}$s of W-DY at those temperatures we find enhancements of 0.45 GN m^{-3} (7%) and 1.00 GN m^{-3} (42%), respectively, presumably due to the operation of an additional mechanism. As suggested in [28] an upward shift in the entire $F_p(b)$ curve will follow an increase in the connectivity. We find evidence that this is happening based on the sharpness of the superconducting transitions, parameterized by $\Delta B \equiv (B_{c2} - B_{irr})/B_{c2}$. From the B_{c2} and

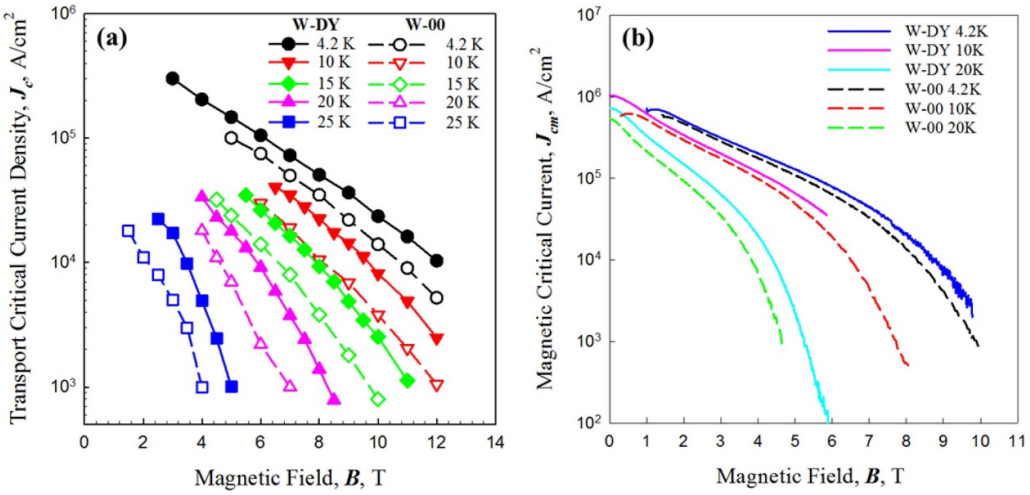

Figure 9. (a) Transport critical current density J_{ct} versus B for W-00 and W-DY at 4.2–25 K; (b) magnetic critical current density J_{cm} versus B for W-00 and W-DY at 4.2–25 K.

Table 6. Increases in J_c at 6 and 4 T that result from Dy_2O_3 doping.

	6 T J_c, 10^4 A cm^{-2}			4 T J_c, 10^3 A cm^{-2}
	4.2 K	10 K	20 K	25 K
W-00	7.50	3.02	2.19	1.0
W-DY	11.6	4.68	9.06	5.0
J_c increase	55%	55%	314%	500%

B_{irr} plots of figures 3(b) and 8 (resistivity data), respectively, we find: (i) at 10 K, $\Delta B_{W\text{-}00} = 0.164$ and $\Delta B_{W\text{-}DY} = 0.111$; (ii) at 20 K, $\Delta B_{W\text{-}00} = 0.170$ and $\Delta B_{W\text{-}DY} = 0.111$; at 25 K, $\Delta B_{W\text{-}00} = 0.328$ and $\Delta B_{W\text{-}DY} = 0.099$, in other words decreases of ΔB at 10 K, 20 K, and 25 K of 32%, 35%, and 70%, respectively. This sharpening of the normal/superconductor transition (reduction in ΔB) that accompanies Dy_2O_3 doping indicates reductions in magnetocrystalline anisotropy (assuming a constant percolation threshold, and material homogeneity). When considering current transport through a polycrystalline superconductor in a magnetic field this allows more crystals to come into play, i.e. increases the connectivity, hence $J_c(B)$ and $F_p(B)$. For example, the $J_c(B)$ plots of figure 9(b), and the corresponding data of table 6 derived from it, show that substantial increases in $J_c(B)$ accrue from the combined influences of Dy_2O_3-doping induced reductions in grain size and increases in connectivity.

4. Summary and discussion

Bulk samples of MgB_2 both undoped and doped with 0.5 wt% of the REOs Nd_2O_3 and Dy_2O_3 (named B-00, B-ND and B-DY, respectively) were prepared by standard powder processing. MgB_2 wires both with and without with the addition of 0.5 wt% Dy_2O_3 (denoted W-00 and W-DY, respectively) were prepared by the CTFF powder-in-tube process. Both W-00 and W-DY used a boron powder pre-doped with C (2% C). Selected samples were characterized using x-ray diffractometry, SEM, TEM, and by magnetic measurement of superconducting transition temperature (T_c) and its width (ΔT_c), magnetic and resistive measurements of upper critical field (B_{c2}) and irreversibility field (B_{irr}), and by magnetic and transport measurements of critical current densities versus applied field, $J_{cm}(B)$ and $J_c(B)$, respectively.

X-ray diffractometry of B-00, B-ND, and B-DY showed no changes in the c and a lattice parameters (figure 1) indicating that the products of REO doping did not substitute into the MgB_2 lattice. The observed invariance of T_c and ΔT_c (figure 2) substantiated that conclusion and provided a reason for the invariance of B_{c2} among B-00, B-ND, and B-DY (figure 3(a)) as well as W-00 and W-DY (figure 3(b)). Although atomic substitution was absent TEM images of B-ND and B-DY showed nanosize inclusions within grains and larger ones outside them (figure 6). The in-grain nano-inclusions evidently did not provide point-defect pinning (figure 10(b)) but the grain-boundary ones seemed to have inhibited grain growth and suppressed grain coarsening (perhaps a Zener pinning mechanism) during HT. Evidence of grain refinement by REO doping is seen in fracture-SEM images of B-00, B-ND, B-DY (figure 4) and those of W-00 and W-DY (figure 5). That undoped and doped MgB_2 are grain-boundary pinners is shown by the forms of the $F_p(b)$ curves that maximize close to $b = 0.2$ (figure 10, tables 2 and 3) and by the proportionality of $F_{p,max}$ to $1/D$ (figures 11 and 12). It is deduced that doping-induced grain refinement is contributing to the observed increases in $J_c(B)$, $J_{cm}(B)$ (figure 9), $F_p(b)$ (figure 10), and $F_{p,max}$ (figures 11 and 12).

Returning to figure 10(a) we note an 8% increase in $F_{p,max}$ (4.2 K) after Dy_2O_3 doping which, as a useful starting point, we attribute to the grain refinement. Application of this 8% increase to the undoped $F_{p,max}$s at 10 and 20 K leaves 7% (at 10 K) and 42% (at 20 K) unaccounted for. By way of explanation we turn to the observed doping-induced increase in B_{irr}; figure 8 shows a 1 T increase in the B_{irr} of the Dy_2O_3-doped wire W-DY over the entire temperature range of measurement,

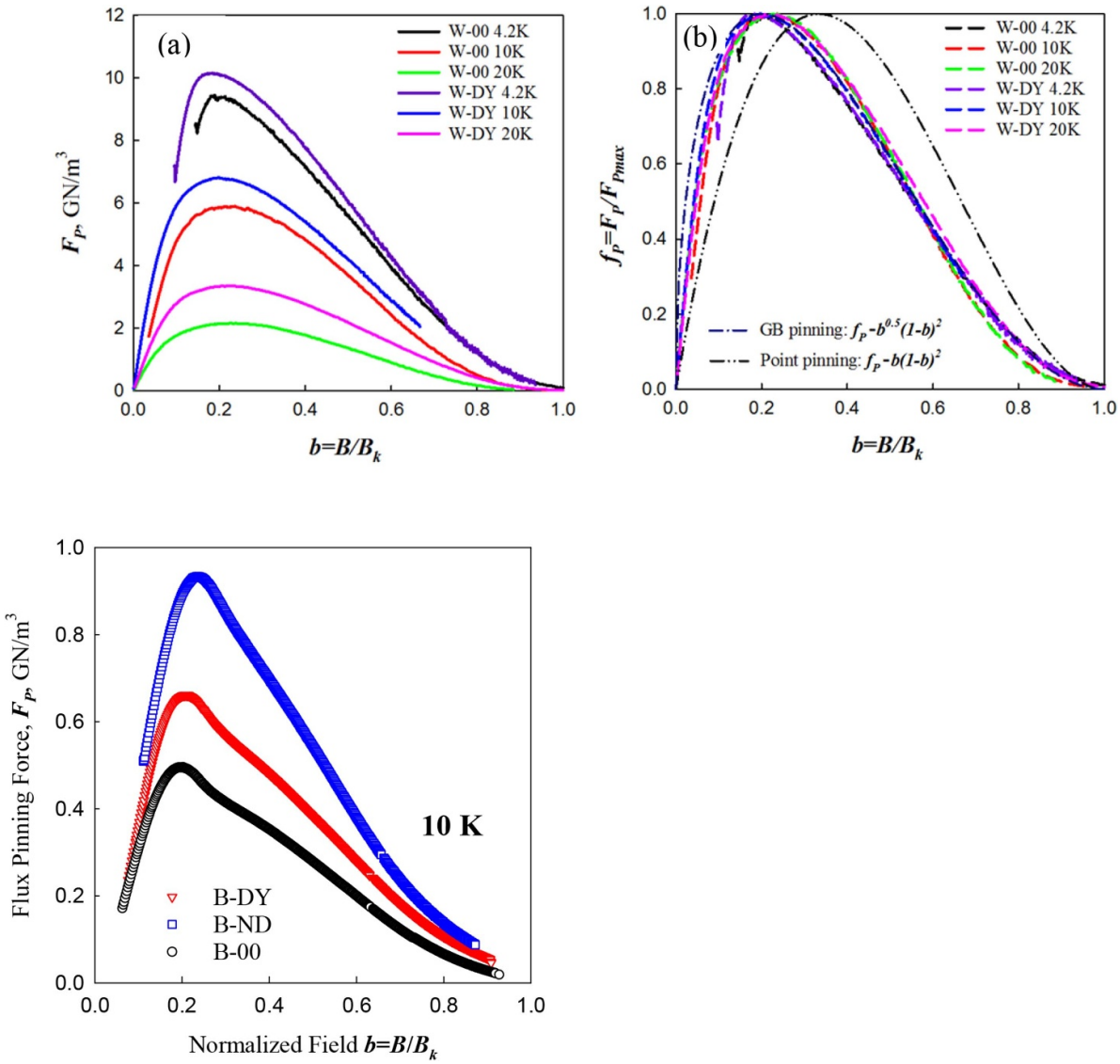

Figure 10. (a) Flux pinning density F_p versus B/B_k for W-00 and W-DY at 4.2–20 K; (b) normalized flux pinning density f_p versus b for W-00 and W-DY at 4.2–20 K. Grain-boundary- and point-pinning functions from [21] are plotted for comparison; (c) flux pinning density F_p versus b at 10 K for B-00, B-ND, and B-DY.

4–25 K. After extracting data from figure 9(a) (as in table 6) we note doping-induced J_c increases (ΔJ_c) of 55% (at 4.2 and 10 K), 314% (20 K), and 500% (25 K). We expect that, beyond grain refinement, increases in B_{irr} make important contributions to ΔJ_c. Then viewing figure 9(a) from a different perspective, the field corresponding to a J_c of 10^4 A cm^{-2} increases by an average of 1.4 ± 0.2 T at all temperatures from 4.2 to 25 K. The ΔB_{irr} of ~1 T would again be a significant contributor to this effect.

As stated above, an increase in B_{irr} translates into: (i) an increase in the operating field range for a given $J_c(T)$, (ii) an increase in J_c at a given B and T, the mechanism for which has to do with anisotropy and connectivity. MgB_2 is a superconductor characterized by a B_{c2} anisotropy parameter $\gamma \equiv B_{c2}{}^{a,b}/B_{c2}{}^{c}$ [29–31]. Since it can be shown that $J_c(B)$ drops more and more steeply as γ increases typically from 1 (isotropic) to 5 or so [29, 30], dopants that decrease γ are sought. Reduction in anisotropy is accompanied by a sharpening of the superconducting/normal transition which we parameterize here by $\Delta B \equiv (B_{c2}-B_{irr})/B_{c2}$. Doping by Dy_2O_3 draws B_{irr} closer to the fixed B_{c2} and reduces ΔB. For example, based on the plots of figures 3(b) and 8 (resistivity data), we find at 10 K $\Delta B_{W\text{-}00} = 0.164$ and $\Delta B_{W\text{-}DY} = 0.111$; a 32% decrease, and at 20 K, and 25 K, decreases of 35%, and 70%, are observed. In the context of current transport through a polycrystalline material in a magnetic field, decreasing the anisotropy would allow more crystals to come into play, i.e. increase the connectivity. The data of table 6 show that Dy_2O_3 doping produces substantial increases in $J_c(B)$ from the combined influences of grain size reduction and increased connectivity. Furthermore the increase in B_{irr} itself extends the range of applicability of MgB_2 conductors.

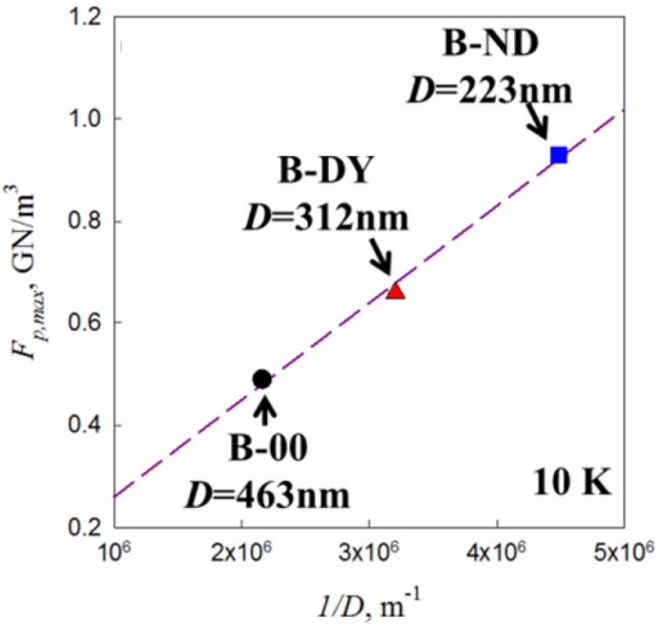

Figure 11. $F_{p,max}$ versus reciprocal grain size, *1/D,* for B-00, B-DY, and B-ND.

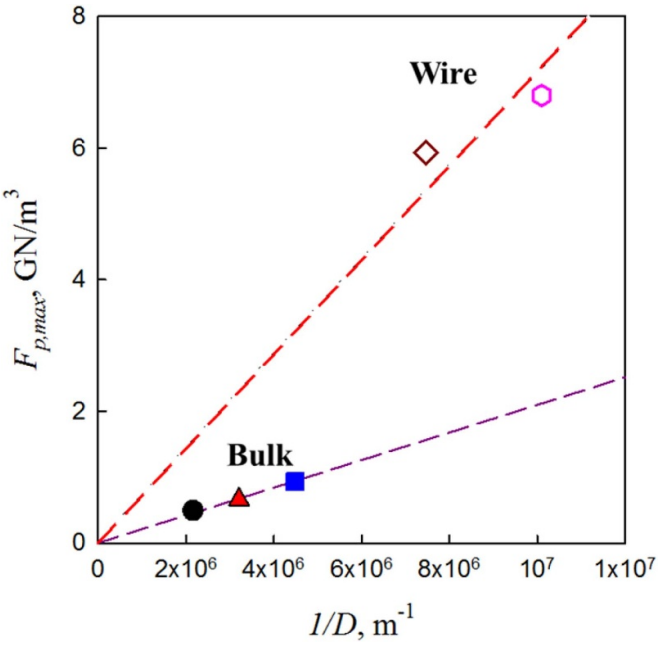

Figure 12. $F_{p,max}$ versus reciprocal grain size, *1/D*, for the bulks B-00, B-ND, and B-DY (lower line) and the wires W-00 and W-DY (upper line).

5. Conclusion

Bulk samples of MgB_2 doped with 0.5 wt% of the REOs Nd_2O_3 and Dy_2O_3 prepared by standard powder processing and wires of MgB_2 doped with 0.5 wt% Dy_2O_3 prepared by a commercial powder-in-tube processing were studied by x-ray diffractometry, scanning- and transmission electron microscopy, magnetic measurement of superconducting transition temperature (T_c), magnetic and resistive measurements of upper critical field (B_{c2}) and irreversibility field (B_{irr}), and magnetic and transport measurements of critical current densities versus applied field ($J_{cm}(B)$ and $J_c(B)$, respectively). Curves of bulk pinning force density (F_p) versus reduced field ($b = B/B_{irr}$) indicating that flux pinning was by grain boundaries, not point defects. At all temperatures the $F_p(b)$ of W-DY experienced enhancement by inclusion-induced grain boundary refinement but at higher temperatures $F_p(b)$ was still further increased by a doping induced increase in B_{irr} of about 1 T at all temperature up to 20 K and beyond. This implies a reduction in the anisotropy, which should also increase percolation and thus J_c. It is noted that Dy_2O_3 increases B_{irr} and that it does so, not just at 4 K, but in the higher temperature regime. In this work, we argue that this increase is due to a reduction in anisotropy. In any case, further optimization of this effect has the potential to expand the range of MgB_2 utility.

Acknowledgments

This work was supported by the NIH, National Institute of Biomedical Imaging and Bioengineering, under R01EB018363, and an NIH bridge grant. A portion of this work was performed at the National High Magnetic Field Laboratory, which is supported by National Science Foundation Cooperative Agreement No. DMR-1157490 and the State of Florida.

ORCID iD

M D Sumption https://orcid.org/0000-0002-4243-8380

References

[1] Dou S X *et al* 2007 Mechanism of enhancement in electromagnetic properties of MgB_2 by nano SiC doping *Phys. Rev. Lett.* **98** 097002
[2] Susner M A, Sumption M D, Bhatia M, Peng X, Tomsic M J, Rindfleisch M A and Collings E W 2007 Influence of Mg/B ratio and SiC doping on microstructure and high field transport J_c in MgB_2 strands *Physica* C **456** 180–7
[3] Susner M A, Yang Y, Sumption M D, Collings E W, Rindfleisch M A, Tomsic M J and Marzik J V 2011 Enhanced critical fields and superconducting properties of pre-doped B powder-type MgB_2 strands *Supercond. Sci. Technol.* **24** 012001
[4] Bohnenstiehl S D, Susner M A, Yang Y, Collings E W, Sumption M D, Rindfleisch M A and Boone R 2011 Carbon doping of MgB_2 by toluene and malic-acid-in-toluene *Physica* C **471** 108–11
[5] Yang Y, Susner M A, Sumption M D, Rindfleisch M, Tomsic M and Collings E W 2012 Influence of strand design, boron type, and carbon doping method on the transport properties of powder-in-tube $MgB_{2-x}C_x$ strands *IEEE Trans. Appl. Supercond.* **22** 6200110
[6] Susner M A, Bohnenstiehl S D, Dregia S A, Sumption M D, Yang Y, Donovan J J and Collings E W 2014 Homogeneous carbon doping of magnesium diboride by high-temperature, high-pressure synthesis *Appl. Phys. Lett.* **104** 162603
[7] Martinelli A, Tarantini C, Lehmann E, Manfrinetti P, Palenzona A, Pallecchi I, Putti M and Ferdeghini C 2008 Direct TEM observation of nanometric-sized defects in

neutron-irradiated MgB_2 bulk and their effect on pinning mechanisms *Supercond. Sci. Technol.* **21** 012001
[8] Martínez E, Mikheenko P, Martínez-López M, Millán A, Bevan A and Abell J S 2007 Flux pinning force in bulk MgB_2 with variable grain size *Phys. Rev.* B **75** 134515
[9] Flükiger R, Hossain M S A and Senatore C 2009 Strong enhancement of J_c and B_{irr} in binary *in situ* MgB_2 wires after cold high pressure densification *Supercond. Sci. Technol.* **22** 085002
[10] Yamada H, Igarashi M, Nemoto Y, Yamada Y, Tachikawa K, Kitaguchi H, Matsumoto A and Kumakura H 2010 Improvement of the critical current properties of in situ powder-in-tube processed MgB_2 tapes by hot pressing *Supercond. Sci. Technol.* **23** 045030
[11] Hur J M, Togano T, Matsumoto A, Kumakura H, Wada H and Kimura K 2008 Fabrication of high-performance MgB_2 wires by an internal Mg diffusion process *Supercond. Sci. Technol.* **21** 032001
[12] Li G Z, Yang Y, Susner M, Sumption M D and Collings E W 2012 Critical current densities and *n*-values of MgB_2 strands over a wide range of temperatures and fields *Supercond. Sci. Technol.* **25** 025001
[13] Li G Z, Sumption M D, Rindfleisch M A, Thong C J, Tomsic M J and Collings E W 2014 Enhanced higher temperature (20–30 K) transport properties and irreversibility field in nano-Dy_2O_3 doped advanced internal Mg infiltration processed MgB_2 composites *Appl. Phys. Lett.* **105** 112603
[14] Chen S K, Wei M and MacManus-Driscoll J L 2006 Strong pinning enhancement in MgB_2 using very small Dy_2O_3 additions *Appl. Phys. Lett.* **88** 192512
[15] Mikheenko P, Chen S K and MacManus-Driscoll J L 2007 Minute pinning and dping additions for strong, 20 K, in-field critical current improvement in MgB2 *Appl. Phys. Lett.* **91** 202508
[16] Yao C, Zhang X, Wang D, Gao Z, Wang L, Qi Y, Wang C, Ma Y, Awaji S and Watanabe K 2011 Doping effects of Nd_2O_3 on the superconducting properties of powder-in-tube MgB_2 tapes *Supercond. Sci. Technol.* **24** 055016
[17] Cheng C and Zhao Y 2006 Enhancement of critical current density of MgB_2 by doping Ho_2O_3 *Appl. Phys. Lett.* **89** 252501
[18] Ojha N, Malik V K, Singla R, Bernhard C and Varma G D 2010 The effect of carbon and rare earth oxide co-doping on the structural and superconducting properties of MgB_2 *Supercond. Sci. Technol.* **23** 045005
[19] Aldica G, Popa S, Enculescu M, Batalu D, Miu L, Ferbinteanu M and Badica P 2014 Addition of Ho_2O_3 of different types to MgB_2 in the ex-situ spark plasma sintering: simultaneous control of the critical current density at low and high magnetic fields *Mater. Chem. Phys.* **146** 313–23
[20] Batalu D, Aldica G, Burdusel M and Badica P 2015 Short review on rare earth and metalloid oxide additions to MgB2 as a candidate superconducting material for medical applications *Key Eng. Mater.* **638** 357–62
[21] Collings E W, Lee E, Sumption M D and Tomsic M 2002 Transport and magnetic properties of continuously processed MgB_2 *Rare Met. Mater. Eng.* **31** 406–9
[22] Marzik J V, Suplinskas R J, Wilke R H T, Canfield P C, Finnemore D K, Rindfleisch M, Margolies J and Hannahs S T 2005 Plasma synthesized doped B powders for MgB_2 superconductors *Physica* C **423** 83–88
[23] Dudni E M, Kocherzhinsky Y A, Paderno Y B, Shitsevalova N Y, Shishkin E A and Kir'yakova I E 1979 Preparation and properties of boride phases of dysprosium *J. Less-Common Met.* **67** 281–5
[24] Susner M A, Daniels T W, Sumption M D, Rindfleisch M A, Thong C J and Collings E W 2012 Drawing induced texture and the evolution of superconductive properties with heat treatment time in powder-in-tube *in situ* processed MgB_2 strands *Supercond. Sci. Technol.* **25** 065002
[25] Dew-Hughes D 1974 Flux pinning mechanisms in type II superconductors *Phil. Mag.* **30** 293–305
[26] Kramer E J 1973 Scaling laws for flux pinning in hard superconductors *J. Phys. D: Appl. Phys.* **44** 1360–70
[27] Mudgel M, Sharath Chandra L S, Ganesan V, Bhalla G L, Kishan H and Awana V P S 2009 Enhanced critical parameters of nanocarbon doped MgB_2 superconductor *J. Appl. Phys.* **106** 033904
[28] Collings E W, Sumption M D, Bhatia M, Susner M A and Bohnenstiehl S D 2008 Prospects for improving the intrinsic and extrinsic properties of magnesium diboride superconducting strands *Supercond. Sci. Technol.* **121** 103001
[29] Eisterer M, Zehetmayer M and Weber H W 2003 *Phys. Rev. Lett.* **90** 247002 4
[30] Susner M A 2012 Chapter 5 PhD Thesis The Ohio State University
[31] Daghero D, Gonnelli R S, Ummarino G A, Stepanov V A, Jun J, Kazakov S M and Karpinski J 2003 Point-contact spectroscopy in MgB_2 single crystals in magnetic field *Physica* C **385** 255–62